

## Article

# Estimation of Daily Potential Evapotranspiration in Real-Time from GK2A/AMI Data Using Artificial Neural Network for the Korean Peninsula

Jae-Cheol Jang , Eun-Ha Sohn, Ki-Hong Park and Soobong Lee 

National Meteorological Satellite Center, Korea Meteorological Administration, Jincheon 27803, Korea; ehsohn@korea.kr (E.-H.S.); parkkihong@korea.kr (K.-H.P.); sblee88@korea.kr (S.L.)

\* Correspondence: jaechool00@korea.kr; Tel.: +82-07-7850-5915

**Abstract:** Evapotranspiration (ET) is a fundamental factor in energy and hydrologic cycles. Although highly precise in-situ ET monitoring is possible, such data are not always available due to the high spatiotemporal variability in ET. This study estimates daily potential ET (PET) in real-time for the Korean Peninsula, via an artificial neural network (ANN), using data from the GEO-KOMPSAT 2A satellite, which is equipped with an Advanced Meteorological Imager (GK2A/AMI). We also used passive microwave data, numerical weather prediction (NWP) model data, and static data. The ANN-based PET model was trained using data for the period 25 July 2019 to 24 July 2020, and was tested by comparing with in-situ PET for the period 25 July 2020 to 31 July 2021. In terms of accuracy, the PET model performed well, with root-mean-square error (RMSE), bias, and Pearson's correlation coefficient ( $R$ ) of  $0.649 \text{ mm day}^{-1}$ ,  $-0.134 \text{ mm day}^{-1}$ , and  $0.954$ , respectively. To examine the efficiency of the GK2A/AMI-derived PET data, we compared it with in-situ ET measured at flux towers and with MODIS PET data. The accuracy of the GK2A/AMI-derived PET, in comparison with the flux tower-measured ET, showed RMSE, bias, and Pearson's  $R$  of  $1.730 \text{ mm day}^{-1}$ ,  $1.212 \text{ mm day}^{-1}$ , and  $0.809$ , respectively. In comparison with the in-situ PET, the ANN model produced more accurate estimates than the MODIS data, indicating that it is more locally optimized for the Korean Peninsula than MODIS. This study advances the field by applying an ANN approach using GK2A/AMI data and could play an important role in examining hydrologic energy for air-land interactions.



**Citation:** Jang, J.-C.; Sohn, E.-H.; Park, K.-H.; Lee, S. Estimation of Daily Potential Evapotranspiration in Real-Time from GK2A/AMI Data Using Artificial Neural Network for the Korean Peninsula. *Hydrology* **2021**, *8*, 129. <https://doi.org/10.3390/hydrology8030129>

Academic Editors: Aristoteles Tegos and Nikolaos Malamos

Received: 14 July 2021

Accepted: 23 August 2021

Published: 27 August 2021

**Publisher's Note:** MDPI stays neutral with regard to jurisdictional claims in published maps and institutional affiliations.



**Copyright:** © 2021 by the authors. Licensee MDPI, Basel, Switzerland. This article is an open access article distributed under the terms and conditions of the Creative Commons Attribution (CC BY) license (<https://creativecommons.org/licenses/by/4.0/>).

**Keywords:** evapotranspiration; GK2A/AMI; artificial neural network; Korean Peninsula

## 1. Introduction

Evapotranspiration (ET) reflects fundamental components of hydrologic and energy cycles of the Earth and is a key element in hydrological resource management [1]. As climate change has progressed, trends in drought and flood have shown different spatial variability, and the importance of hydrological system monitoring has been emphasized [2]. Accordingly, it is fundamental to quantify and monitor ET. However, since water resources are directly affected by regional hydrologic systems and meteorology, ET shows high spatial and temporal variability [3].

A major application of ET is drought monitoring. Climate change has altered drought trends, increasing the intensity, frequency, and extent of droughts [4]. Thereafter, numerous indices for drought monitoring have been developed, with several, such as the standardized precipitation evapotranspiration index [5], precipitation evapotranspiration difference condition index [6], reconnaissance drought index [7], and combined terrestrial evapotranspiration index [8], directly associated with ET. Based on these drought indices, many studies were conducted to investigate the long-term variability of water budget under specific climate change conditions [9], effects of climate elasticity of ET on water balance [10], spatiotemporal variability of drought characteristics [11], and impacts of

drought events on agricultural production [12]. In addition to various applications of ET, the methods to estimate ET with higher accuracy and spatiotemporal resolution have also been studied.

ET can be classified depending on the soil moisture condition. Potential ET (PET) is defined as the water vapor transpired and evaporated from vegetation and soil in unlimited soil moisture conditions [13]. Actual ET (AET) represents the water vapor transferred from a surface under limited soil moisture conditions. Weighing lysimeters are the most accurate AET measuring instruments [14]. Although they measure AET directly, the available AET data are substantially limited for end-users [15]. To ensure the versatility of ET data, various ET estimating models have been developed that can be broadly classified into three types [16]: (1) fully physical combination models that deal with mass and energy transfer principles [17,18]; (2) semi-physical models that account for mass or energy transfer principles and are based on temperature and radiation [19,20]; and (3) black-box models that are based on empirical relationship, artificial neural networks (ANN), fuzzy, and genetic algorithm. Although there are various ET estimating models, the most widely used method is the Penman–Monteith (PM) method [21,22]. The PM method is a fully physical model developed by Penman [17] and later modified by Monteith [18]. This model is recommended as the global reference model for ET monitoring by the Food and Agriculture Organization of the United Nations (FAO).

Although in-situ ET measurements are highly precise, the spatial variability of ET is high, and the availability of in-situ ET measurements is limited [23]. Remotely sensed data have been used to address this problem. Satellite data have broad spatial coverage with high temporal resolution and produce reliable products [24]. MODerate resolution Imaging Spectroradiometer (MODIS) derives the operative ET products with 500 m spatial and 8-days temporal resolution [25]. Several studies have estimated the spatial distribution of ET using low Earth orbit (LEO) satellites with optical-infrared and microwave sensors [26,27]. When calculating ET using LEO satellites, external input data, such as meteorological data, are generally necessary [28]. In particular, because LEO satellites observe the Earth's surface at specific local times, it is difficult for the instantaneous observation to monitor the environmental conditions all day and all weather [29]. Therefore, due to the high temporal variability of ET, LEO satellite-derived ET has inevitable limitations for routine monitoring of daily ET and surface energy fluxes [11,30]. In addition, since LEO satellites apply the physical-based model or energy conservation-based model for estimating ET, there exist uncertainties of external input data for applying the model [25–27]. Using geostationary orbit (GEO) satellites data can compensate for the limitations associated with the temporal resolution of LEO satellite data. However, it is difficult to resolve the uncertainties of external input data and the data contaminated by weather conditions, including clouds and aerosols [29].

The Korean Peninsula is located on the margin of Northeast Asia, bordering the northwest Pacific Ocean (Figure 1a). Since it is located in a monsoon region, where meteorological droughts occur during the summer monsoon, the droughts tend to propagate into agricultural or hydrological droughts [31]. In particular, the Korean Peninsula land cover type showed complex spatial distribution comprising of diverse vegetation cover types (Figure 1b). Furthermore, in the Korean Peninsula, the drought frequency has increased, and drought trends and characteristics vary regionally [32]. The Korean Peninsula has various land cover types and specific terrain properties; these factors make it particularly difficult to monitor daily ET even employing both in-situ measurement and remotely sensed data. Due to frequent cloud cover and rainfall, it is challenging to observe the land surface using optical-infrared satellites in the summer monsoon season [33]. Therefore, to overcome this limitation, numerical model data and ancillary data have been used to retrieve ET [34,35].

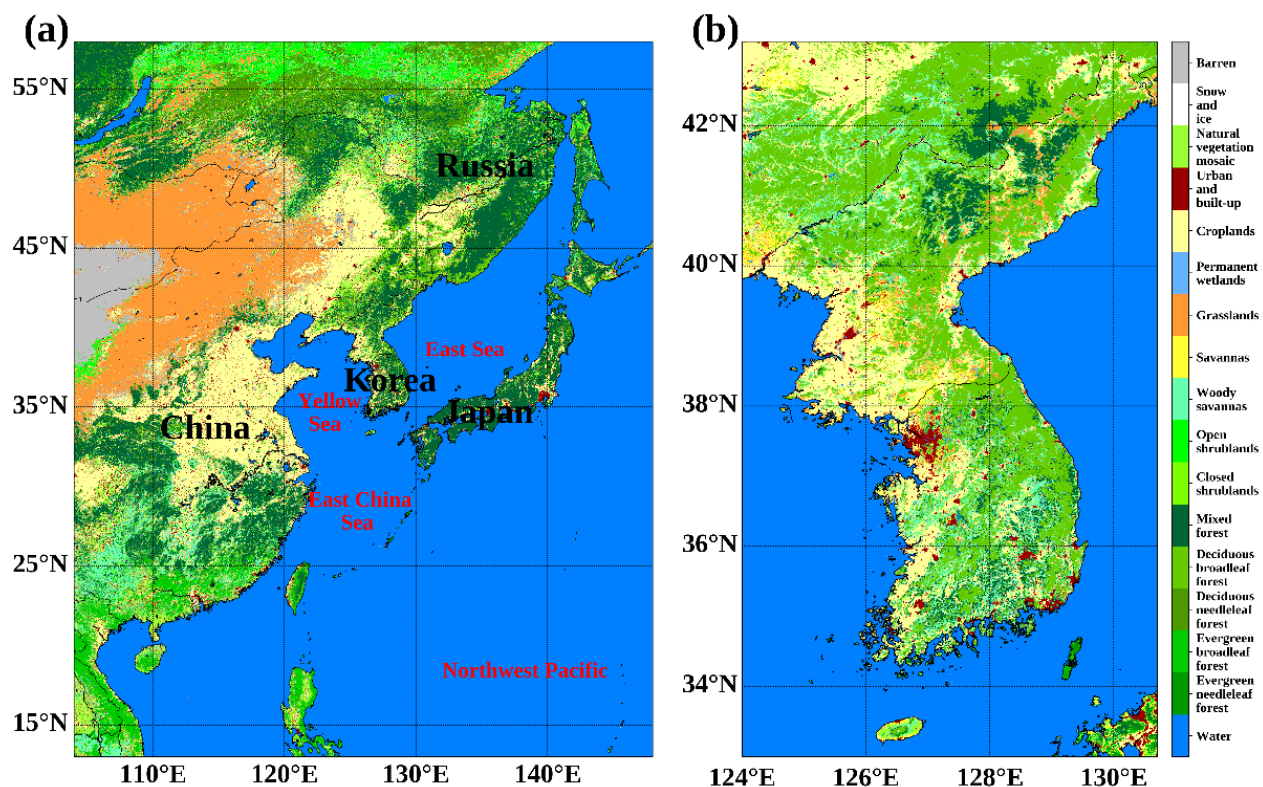


**Figure 1.** MODIS land cover from the Annual International Geosphere-Biosphere Programme over (a) Northeast Asia and (b) the Korean Peninsula in 2019.

In order to manage hydrological resources over the Korean Peninsula, Korea Meteorological Administration (KMA) monitors the ET in real-time using in-situ measurements and numerical model data. In-situ measurements exhibit good performance with high temporal resolution every hour; however, its availability is limited due to the point observation. For complementing the limitation of in-situ measurements, KMA calculates the spatial distribution of ET using numerical model data based on geophysical models. Numerical model data-derived ET is suitable for analyzing droughts with a large time scale. In contrast, the accuracy of the ET changes depending on the numerical model data, and it is difficult to calculate the ET that reflects various topographical characteristics of the Korean Peninsula due to the sparse spatial resolution of the numerical model data.

Although physical-based models show good performance, due to numerous associated meteorological parameters, it is difficult to estimate accurate ET, especially in remote sensing applications. Then, over the last few decades, many researchers have identified that machine learning (ML) approaches were an effective method to overcome the complexity of ET estimation [29]. Because ML techniques solve the non-linear relationship between input and output variables, a lot of ML techniques have been proposed to estimate ET for hydrological applications [36], such as k-nearest neighbors [37], support vector machine [38], random forest [37], and artificial neural network (ANN) [39]. Previously, most studies applied ML approaches to in-situ measurements; however, many recent studies have also applied ML approaches to remote sensing data [40–42].

In this study, considering the spatiotemporal variability in ET, we developed a model that estimates daily PET based on ANN using the GEOstationary Korea Multi-Purpose SATellite 2A (GEO-KOMPSAT 2A, GK2A). The objective was to retrieve real-time daily ET with a spatial resolution of 1 km for hydrological resource monitoring on the Korean Peninsula. To reflect the complex relationships and nonlinearity between the GK2A-derived data and ET, we used precipitation data and the digital elevation data as input data for the ANN. Daily PET from KMA was used as reference data for ANN model training.

The accuracy of the model was verified by comparing modeled data with ET from in-situ measurements of the KMA and National Institute of Forest Science (NIFoS) for the period excluding the period of training data.

## 2. Data and Methods

### 2.1. Remote Sensing Data

#### 2.1.1. GEO-KOMPSAT 2A (GK2A)

GK2A, launched on 4 December 2018 and operated by the KMA National Meteorological Satellite Center (NMSC), is equipped with the Advanced Meteorological Imager (AMI). AMI is the optical-infrared sensor with 16 channels and its spatial resolution ranges from 0.5 to 2.0 km depending on wavelength (Table 1). Since GK2A/AMI observes the Earth with a high spatiotemporal resolution, it is more capable of monitoring the Earth's hydrological system than previous GEO satellite (Communication, Ocean and Meteorological Satellite, COMS) operated by KMA NMSC and other LEO satellites [43]. We used seven GK2A/AMI operational products: Reflected Shortwave Radiation (RSR), Downward Shortwave Radiation (DSR), Absorbed Shortwave Radiation (ASR), Outgoing Longwave Radiation (OLR), Downward Longwave Radiation (DLR), Upward Longwave Radiation (ULR), and Normalized Difference Vegetation Index (NDVI).

**Table 1.** Specifications of the GEO-KOMPSAT 2A Advanced Meteorological Imager (GK2A/AMI) spectral channels.

Channel No.	Channel Name	Wavelength Range ( $\mu\text{m}$ )	Resolution (km)
1	VIS004	0.431–0.479	$1.0 \times 1.0$
2	VIS005	0.5025–0.5175	$1.0 \times 1.0$
3	VIS006	0.625–0.66	$0.5 \times 0.5$
4	VIS008	0.8495–0.8705	$1.0 \times 1.0$
5	NR013	1.373–1.383	$2.0 \times 2.0$
6	NR016	1.601–1.619	$2.0 \times 2.0$
7	SW038	3.74–3.96	$2.0 \times 2.0$
8	WV063	6.061–6.425	$2.0 \times 2.0$
9	WV069	6.89–7.01	$2.0 \times 2.0$
10	WV073	7.258–7.433	$2.0 \times 2.0$
11	IR087	8.44–8.76	$2.0 \times 2.0$
12	IR096	9.543–9.717	$2.0 \times 2.0$
13	IR105	10.25–10.61	$2.0 \times 2.0$
14	IR112	11.08–11.32	$2.0 \times 2.0$
15	IR123	12.15–12.45	$2.0 \times 2.0$
16	IR133	13.21–13.39	$2.0 \times 2.0$

#### 2.1.2. Precipitation Data

Integrated Multi-satellitE Retrievals for Global Precipitation Measurement (IMERG) version 6 were used to calculate ET, even for areas for which precipitation data were not available. The IMERG precipitation products are derived from the global precipitation measurement constellation comprising the various passive microwave sensors including the meteorological operational satellite series, polar operational environmental satellite series, and global change observation mission 1st-water satellite [44]. The data from various passive microwave satellites are merged into  $0.1^\circ \times 0.1^\circ$  resolution every 30 min. We used the standardized precipitation index for six months (SPI6), derived from the precipitation product of IMERG, rather than daily precipitation data.

### 2.2. Numerical Model and Elevation Data

Since 2010, the KMA has used numerical weather prediction (NWP) systems from the Unified Model (UM). NWP model data from UM systems, operated by KMA in real-time, could be classified depending on spatial coverage and boundary conditions, and we used Local Data Assimilation and Prediction System (LDAPS) over the Korean Peninsula in this

study. LDAPS is based on boundary conditions derived by three-dimensional variational data assimilation and its spatial resolution of 1.5 km [45]. LDAPS has 70 vertical layers and provides 36-h predictions (at every 00, 06, 12, and 18 UTC), and additional 3-h predictions (at every 03, 09, 15, and 21 UTC). We used four meteorological parameters—air temperature ( $T_a$ ), surface temperature ( $T_s$ ), relative humidity (RH), and wind speed (WS)—from LDAPS version 10.1. Furthermore, Shuttle Radar Topography Mission (SRTM) digital elevation model (DEM) data were used to reflect the effect of elevation on ET, and its spatial resolution was an arc-second, approximately 30 m [46].

### 2.3. In-Situ Measurements

PM equation calculates the PET using micrometeorological data, and the eddy covariance (EC) systems estimate the AET based on energy flux observations [47]. PET derived from the PM method was used for model training and validation. On the other hand, since the AET derived from EC systems was different from PET, we only used the AET data for testing the availability of the PET model.

Since the Korean Peninsula has specific geographic characteristics, each region shows different weather conditions and climate properties. KMA operates 81 Automated Surface Observing System (ASOS) stations in real-time. In this study, we used 42 of these that monitor  $ET_o$  based on the PM equation (we hereafter refer to ET obtained using the PM equation as PM-ET) (Figure 2a). ASOS stations observe the following meteorological parameters every hour:  $T_a$ ,  $T_s$ , RH, WS, soil temperature, precipitation, surface pressure, and net solar radiation (<https://data.kma.go.kr/cmmn/main.do>, accessed on 13 July 2021).

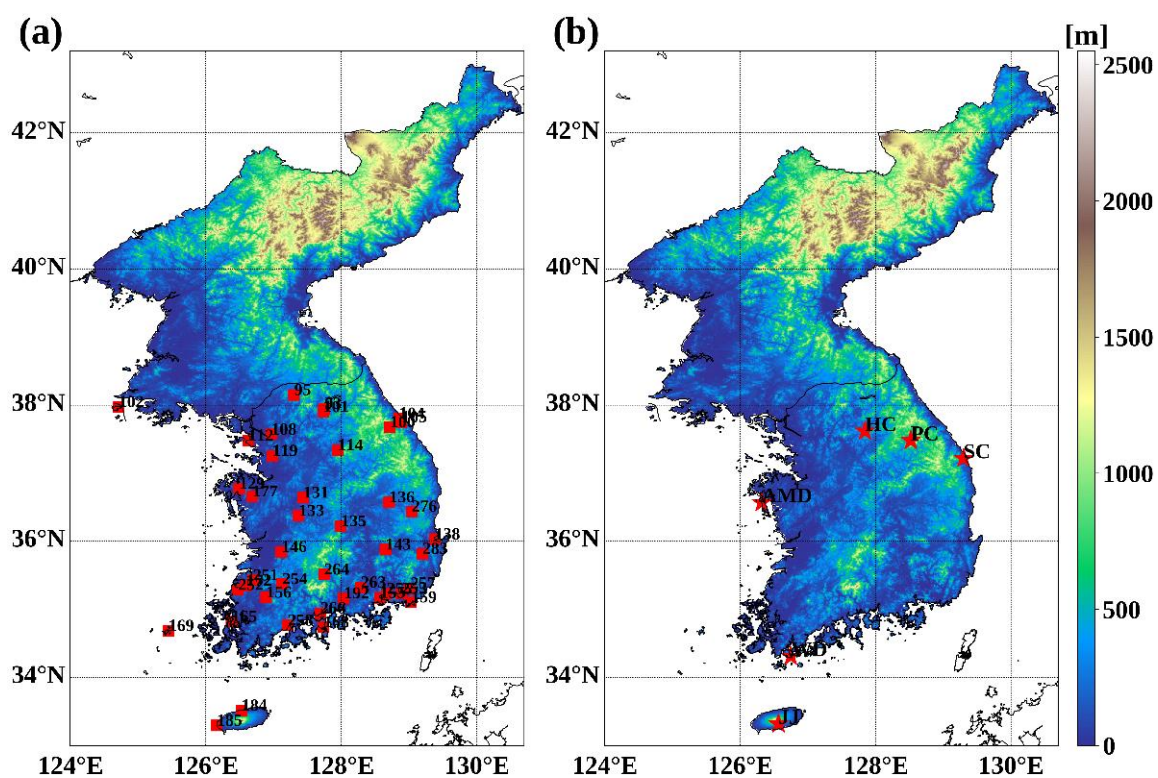


**Figure 2.** Distribution of the digital elevation model (DEM), where the red squares and stars indicate the (a) Automated Surface Observing System (ASOS) stations and (b) flux towers, respectively.

To evaluate the ANN model-derived ET, we used ET calculated using the EC method. The NIFoS operates six flux towers to monitor ET on the Korean Peninsula (Figure 2b). These flux towers observe meteorological parameters every 30 min (<http://know.nifos.go.kr/know/service/flux/fluxIntro.do>, accessed on 13 July 2021). Using these direct observations of vertical flux and meteorological data, it is possible to calculate ET via the

EC method. From the ASOS stations and flux towers, we selected only those variables observed for full 24-h periods.

#### 2.4. Processing

Figure 3 illustrates the process used here to estimate and evaluate daily ET using GK2A/AMI data. We preprocessed the input data; the preprocessed data were then subsampled (at 1 km resolution) around the Korean Peninsula. We constructed matchups between the subsampled data and PM-ET, and classified them into two datasets (training and testing) depending on the acquisition date. For the ANN model training, we used five-fold cross-validation; 80% of the data were used to optimize the weights and biases of the model, and 20% were used to verify the accuracy and monitor the loss function of the model, to minimize overfitting. To enable the ANN model to reflect seasonal variation, we set the training period for the training data to 1 year (25 July 2019 to 24 July 2020). ANN model performance was assessed using PM-ET and EC-ET data for the period 25 July 2019 to 31 July 2021.

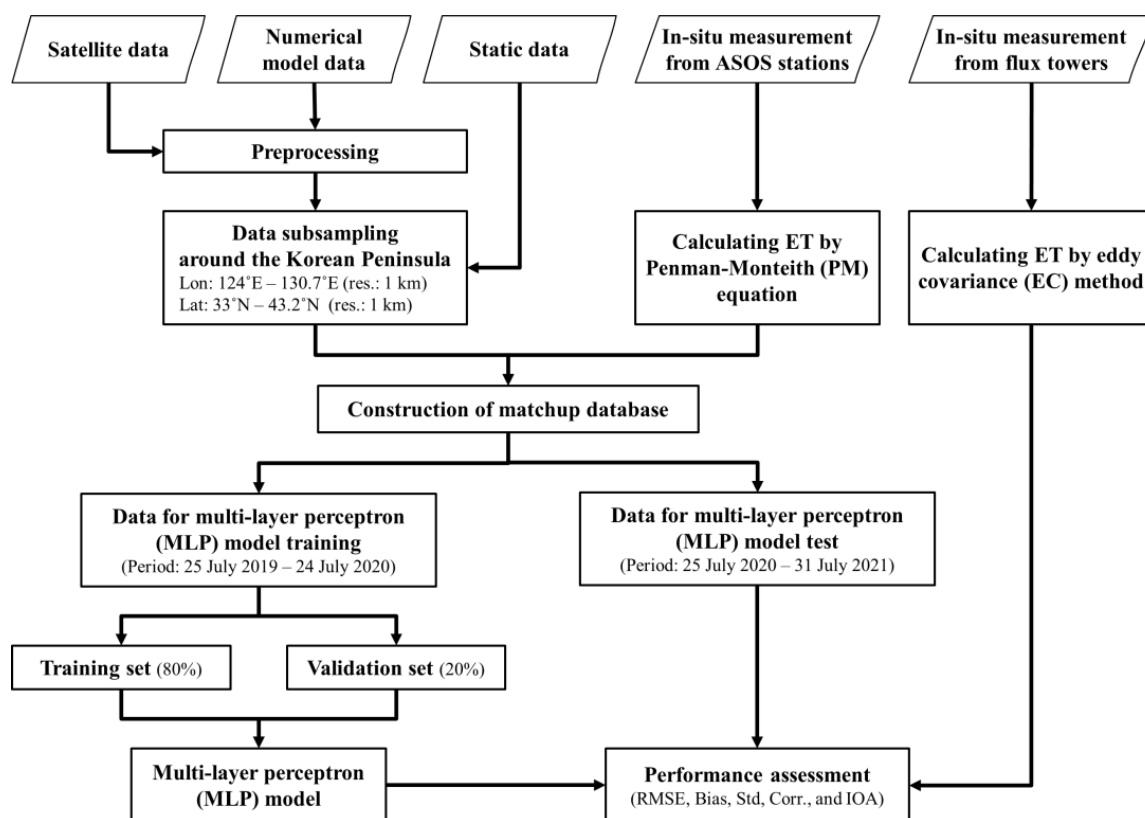


**Figure 3.** Flowchart illustrating the construction and assessment of the evapotranspiration (ET) retrieval artificial neural network (ANN) model.

To estimate daily ET via GK2A/AMI data, we used 22 parameters as input variables of the ANN model (Table 2). The GK2A/AMI operational products include the preprocessed daily means of six radiation variables (RSR, DSR, ASR, OLR, DLR, and ULR) and the 16 days maximum NDVI. The GPM IMERG precipitation product was preprocessed to generate SPI6. We used four UM LDAPS variables (Ta, Ts, RH, and WS) affecting ET. To take into account diurnal variation in ET, we preprocessed NWP variables to daily mean, daily minimum, and daily maximum. As static data, we used extraterrestrial solar radiation (ESR) and a DEM to account for seasonal variation and the terrain effect, respectively.

**Table 2.** Spatial and temporal resolution, processing method, and input data source for the artificial neural network (ANN) model, where Mean, Max, Min, and Sum indicate average, maximum, minimum, and cumulative values, respectively.

Data	Variables	Spatial Resolution (Temporal Resolution)	Processing	Source
GK2A/AMI	RSR DSR ASR OLR DLR ULR	2 km × 2 km (10 min)	<i>Mean<sub>1day</sub></i>	KMA NMSC
	NDVI	2 km × 2 km (1 day)	<i>Max<sub>16days</sub></i>	
GPM IMERG	SPI6	10 km × 10 km (1 day)	<i>Sum<sub>6months</sub></i>	NASA
UM LDAPS	Ta Ts RH WS	1.5 km × 1.5 km (3 h)	<i>Mean<sub>1day</sub></i> , <i>Max<sub>1day</sub></i> , <i>Min<sub>1day</sub></i>	Met Office
Static data	ESR	–	–	–
	DEM	30 m × 30 m	–	NASA

#### 2.4.1. Extraterrestrial Solar Radiation (ESR)

ESR indicates solar radiation incident outside the Earth from the Sun. ESR is a key parameter for estimating ET, and can be calculated using the latitude and the day of the year as follows [21,48]:

$$R_a = \frac{24 \times 60}{\pi} G_{SC} d_r (\omega_S \sin \varphi \sin \delta + \cos \varphi \cos \delta \sin \omega_S), \quad (1)$$

where  $R_a$  refers to ESR;  $G_{SC}$  denotes the solar constant;  $d_r$  represents the inverse of the relative distance between the Earth and the Sun;  $\omega_S$  indicates the Sun and sunset hour angle;  $\varphi$  and  $\delta$  refer to latitude and solar declination, respectively.

#### 2.4.2. Penman–Monteith Evapotranspiration (PM-ET)

We calculated hourly PM-ET from in-situ KMA ASOS station measurements. To account for diurnal variability in ET, we also derived daily PM-ET from hourly PM-ET. It is possible to estimate hourly PM-ET as follows [21]:

$$ET_o = \frac{0.408\Delta(R_n - G) + \gamma \frac{37}{T_{hr} + 273} u_2 (e^o(T_{hr}) - e_a)}{\Delta + \gamma(1 + 0.34u_2)}, \quad (2)$$

where  $ET_o$  indicates hourly ET;  $T_{hr}$  and  $u_2$  represents hourly mean air temperature and hourly mean wind speed, respectively;  $\Delta$  denotes the saturation slope vapor pressure at  $T_{hr}$ ;  $\gamma$  and  $R_n$  denote the psychrometric constant and the net radiation at the surface, respectively;  $G$  and  $e^o$  refer to the soil heat flux density and the saturation vapor pressure at  $T_{hr}$ , respectively;  $e_a$  indicates hourly mean actual vapor pressure. KMA ASOS station calculated hourly PM-ET every hour, and the cumulative PM-ET over 24 h was used as the daily PM-ET.

#### 2.4.3. Standardization of Input Variables

In an ANN model, when the input variables are linearly related, it is not necessary to standardize or normalize them. However, when the input variables show a non-linear relationship in the ANN model, before using input variables, it is important to standardize or normalize them [49]. When using the variables without standardization or normalization, large values of the input variables would cause very small weighting factors, and small

values of the input variables would result in very large weighting factors, which could cause some problems during training and optimizing process [50]; Using extremely small weights would cause the uncertainties of floating-point calculations on computer; not using extremely small initial weights would make the improvement of the model by the backpropagation algorithm insignificantly small [51]. There are no fixed methods of standardization that should be used in specific applications; in this study, standardization was applied to input variables as follows:

$$V' = \frac{(V - V_{mean})}{V_{std}}, \quad (3)$$

where  $V'$  and  $V$  indicate the standardized input variable and unstandardized input variable, respectively;  $V_{mean}$  represents the mean of input variable;  $V_{std}$  denotes the standard deviation of the input variable.

## 2.5. ANN Model

### 2.5.1. Model Structure

We used a multilayer perceptron (MLP), ANN, to estimate daily ET. MLP involves feedforward backpropagation networks with a simple structure and high performance; they have therefore been used for diverse applications using satellite data [52,53]. These neurons are interconnected, with weights and biases that enable repetitive learning. Each hidden layer has an activation function computing the neuronal weights and biases. An optimizer algorithm trains the network and minimizes the error, by correcting the weights and biases via a backpropagation process [54]. We developed a five-layer MLP model with hidden layers of 200 neurons. In MLP model training, input values of neurons in the previous layer transfer to a neuron in the current layer, and a neuron combines the input values with weights and biases as follows [51]:

$$n_j = \sum x_i w_{ij} - b_j, \quad (4)$$

where  $n_j$  represent the net of the weighted input for the  $j$ th neuron;  $x_i$  indicate the input transferred from the  $i$ th neuron;  $w_{ij}$  refers to the weight connected from the  $i$ th neuron to the  $j$ th neuron;  $b_j$  means the bias of the  $j$ th neuron. In  $n_j$ , for being a final output for passing to the next layer, it should be activated by the activation function [49]. The activation function can be a diverse discrete or continuous function; we used the exponential linear unit (ELU), showing fine performance with a fast learning rate and significantly better generalization as follows [55]:

$$f(x) = \begin{cases} x & \text{if } x > 0 \\ \alpha(\exp(x) - 1) & \text{if } x \leq 0 \end{cases} \quad (5)$$

where  $\alpha$  represents the hyperparameter controlling the value where an ELU saturates for negative  $n_j$ ;  $x$  denotes the input value and indicates the  $n_j$ .

For improving and accelerating the convergence, we used the batch normalization (BN) layer between each hidden layer [56]. The normalization is calculated based on the dimension of the batch and BN ensures that the input of each hidden layer is distributed in the same way. Their performance dramatically depends on the batch size, and setting a larger batch size generally yields better performance [57]. We used a method for stochastic optimization (ADAM) as the optimizer algorithm [58]. The parameters and hyperparameters of the MLP model are summarized in Table 3. To train and run the MLP model, we used Keras with the TensorFlow back-end in Python.

**Table 3.** Parameters and hyperparameters of the multilayer perceptron (MLP) model.

Parameter		Hyperparameter	
Activation	ELU	Alpha	1
Optimizer	ADAM	Learning rate	$10^{-4}$
		Beta1	0.9
		Beta2	0.999
		Epsilon	$10^{-7}$
Loss function	RMSE		
Epochs	100		
Batch size	500		

### 2.5.2. Mean Decrease Accuracy (MDA)

In a black-box model such as an ANN model, it is difficult to analyze the information and structure of the model in detail. However, it is possible to rank the importance that each input variable occupies in the model. In this study, in order to analyze the trained MLP model, we conducted a permutation test of each input variable. This test randomly permutes the list of a variable and measures the decrease of model accuracy; this process was conducted repeatedly with each variable; finally, the Mean Decrease Accuracy (MDA; also known as the permutation importance) was calculated with each variable [59]. A variable with a larger MDA is interpreted as an important variable in the model because the accuracy of the variable greatly affects the accuracy of the model. We used the MDA in terms of the increase in RMSE when each variable was randomly permuted.

### 2.6. Statistical Analysis

Daily ET, estimated via MLP, was compared with PM-ET and EC-ET. To quantitatively evaluate the MLP-derived daily ET, we used the bias [60], root-mean-square error (RMSE) [36], mean absolute error (MAE) [36], standard deviation (STD) [60], normalized RMSE (nRMSE) [61], Pearson's correlation coefficient ( $R$ ) [36], and the Index of Agreement (IOA) [62]. The detailed equations are as follows:

$$\text{Bias} = \frac{1}{N} \sum_{i=1}^N (E_i - O_i), \quad (6)$$

$$\text{RMSE} = \sqrt{\frac{\sum_{i=1}^N (E_i - O_i)^2}{N}}, \quad (7)$$

$$\text{MAE} = \frac{1}{N} \sum_{i=1}^N |E_i - O_i|, \quad (8)$$

$$\text{STD} = \sqrt{\frac{\sum_{i=1}^N (E_i - O_i - \text{Bias})^2}{N}}, \quad (9)$$

$$\text{nRMSE} = \frac{\sqrt{\frac{\sum_{i=1}^N (E_i - O_i)^2}{N}}}{\frac{\sum_{i=1}^N O_i}{N}}, \quad (10)$$

$$R = \frac{\sum_{i=1}^N (E_i - \bar{E})(O_i - \bar{O})}{\sqrt{\sum_{i=1}^N (E_i - \bar{E})^2} \sqrt{\sum_{i=1}^N (O_i - \bar{O})^2}}, \quad (11)$$

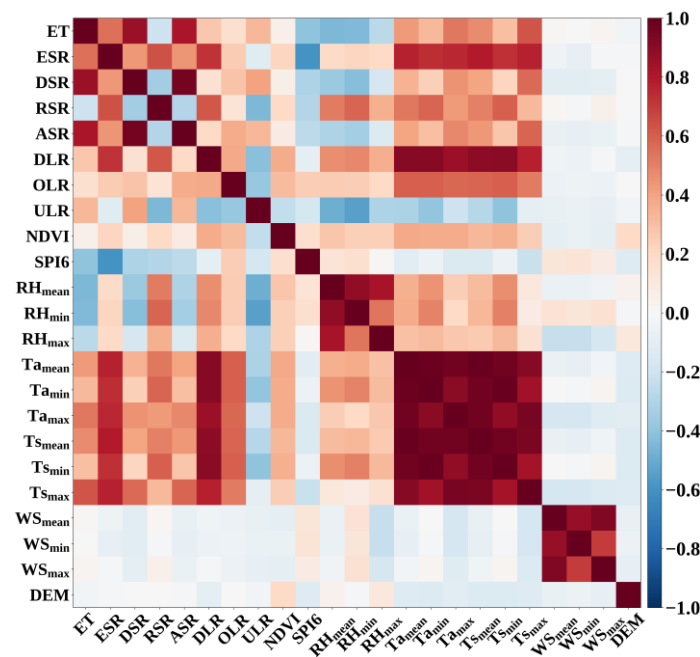
$$\text{IOA} = 1 - \frac{\sum_{i=1}^N (E_i - O_i)^2}{\sum_{i=1}^N (|E_i - \bar{O}| + |O_i - \bar{O}|)^2}, \quad (12)$$

where  $E_i$  and  $O_i$  represent the estimated ET and observed ET, respectively; the subscript  $i$  denotes the  $i$ th data point;  $N$  refers to the number of data;  $\bar{E}$  and  $\bar{O}$  represent the mean of the estimated ET and observed ET, respectively.

### 3. Results

#### 3.1. Input Data Correlation

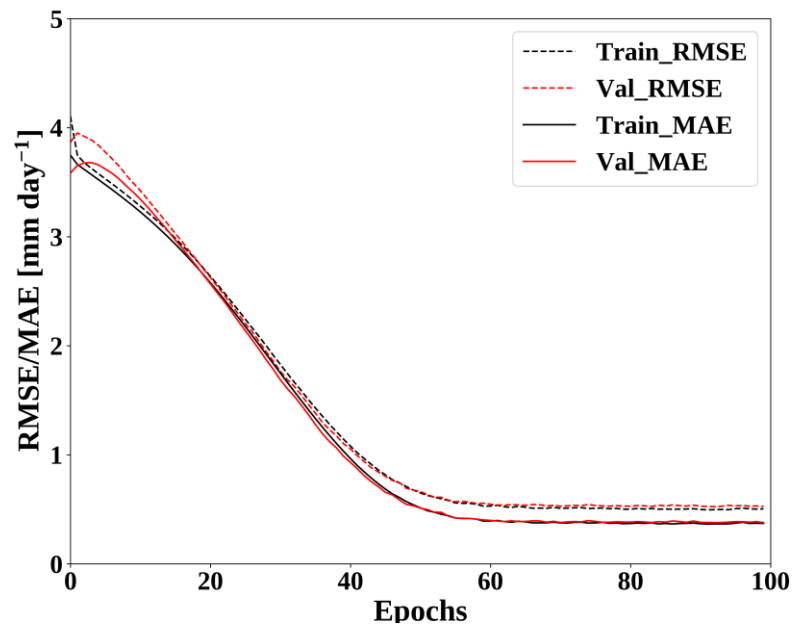
Figure 4 describes the correlations between the input variables used in estimating daily ET, and ET from the KMA ASOS stations, for the Korean Peninsula. Fifteen of the variables (ESR, DSR, ASR, DLR, OLR, ULR, NDVI,  $T_{a\text{mean}}$ ,  $T_{a\text{min}}$ ,  $T_{a\text{max}}$ ,  $T_{s\text{mean}}$ ,  $T_{s\text{min}}$ ,  $T_{s\text{max}}$ ,  $WS_{\text{mean}}$ , and  $WS_{\text{max}}$ ) were positively correlated with daily ET from the KMA ASOS stations. As the radiation incident on the surface and the temperature increases, evaporation increases, because sufficient energy to convert water into water vapor is provided, and transpiration increases because vegetation activity accelerates [63]. Seven variables (i.e., RSR, SPI6,  $RH_{\text{mean}}$ ,  $RH_{\text{min}}$ ,  $RH_{\text{max}}$ ,  $WS_{\text{min}}$ , and DEM) were negatively correlated with daily ET from the KMA ASOS stations. As higher RH is associated with less water vapor transported from the water surface, RH was negatively correlated with ET. Since precipitation increases surface water content and inhibits evaporation, SPI6 was negatively correlated to ET. As RSR increases, the radiation incident on the surface decreases, reducing both evaporation and transpiration. The mean, maximum, and minimum WS showed different correlations with ET; this could be because the complex topography of the Korean Peninsula, in terms of spatiotemporal variability in WS, causes uncertainty of the LDAPS model WS estimates. Overall, the positive correlations were stronger than the negative correlations. Relative to ET, DSR had the strongest positive correlation (0.86), and  $RH_{\text{mean}}$  had the largest negative correlation ( $-0.45$ ).



**Figure 4.** Correlation coefficient between the input variables in the matchups from 25 July 2019 to 24 July 2020.

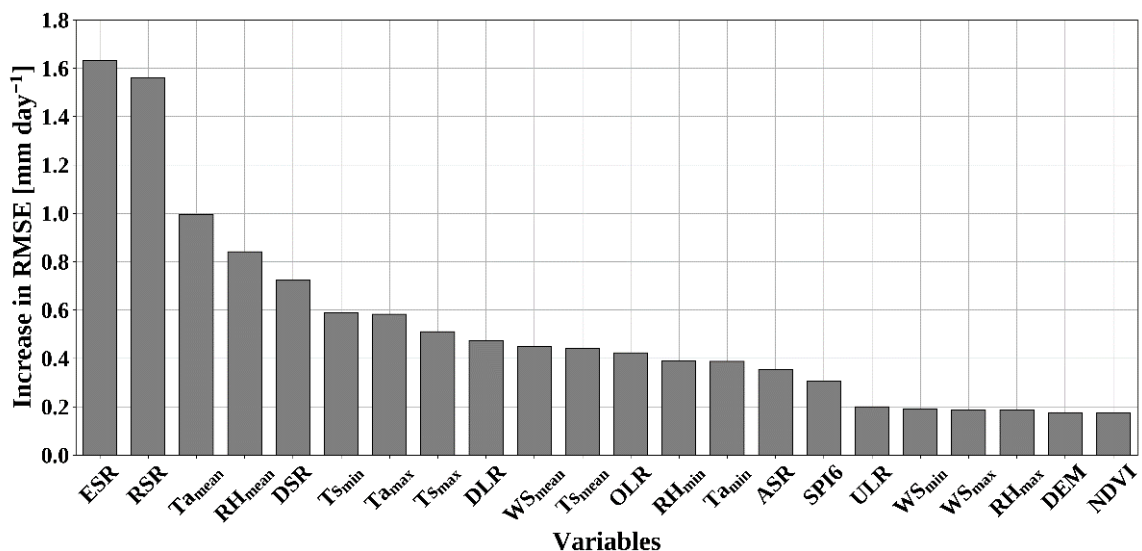
#### 3.2. MLP Model

Figure 5 describes the MLP model training history. Training the MLP model involves minimizing RMSE (the loss function) by optimizing neuronal bias and weight. Up to training epoch 50, RMSE and MAE decreased rapidly, but after epoch 70, the accuracy slightly improved. By training epoch 100, the change in RMSE and MAE of both the training and validation datasets were almost negligible.



**Figure 5.** Changes in RMSE and MAE with respect to the training epochs of the ANN model training epochs, where Red and black lines indicate validation and training data sets, respectively; Dotted and solid lines represent RMSE and MAE, respectively.

Figure 6 shows the MDA of 22 input variables in the ANN model. ESR and RSR showed high MDA ( $>1.5 \text{ mm day}^{-1}$ ), which means that ET is predominantly affected by radiation energy. ESR, which is used directly in the PM equation, showed an MDA of  $1.63 \text{ mm day}^{-1}$ . RSR, which measures the shortwave radiation that emits outside the Earth, is principally controlled by clouds and surface albedo. These land and meteorological conditions directly affect the parameters in the PM equation, which explains the high MDA values of RSR and DSR, at  $1.56$  and  $0.72 \text{ mm day}^{-1}$ , respectively.



**Figure 6.** Mean Decrease Accuracy (MDA), expressed as the increase in RMSE, of ET derived from the ANN model.

Ta, Ts, and RH are directly related to ET estimation, via the PM equation. However, since they are derived from numerical model data with uncertainty, they showed relatively low MDAs, from  $0.99$  to  $0.19 \text{ mm day}^{-1}$ . The variables describing WS, which are used directly in the PM-ET estimation, showed lower MDAs ( $<0.45 \text{ mm day}^{-1}$ ) than the other

meteorological variables. This reflects the fact that it is difficult to simulate transient changes in wind caused by sudden gusts or topography using numerical model-based wind data. PET reflects the rate of ET when sufficient soil moisture is available; hence it does not account for vegetation and terrain characteristics. As a result, NDVI and DEM showed lower MDA values ( $<0.18 \text{ mm day}^{-1}$ ).

### 3.3. Evaluation against KMA Stations

We compared GK2A-derived daily ET for the Korean Peninsula with PM-ET derived from KMA ASOS stations for the period 25 July 2020 to 31 July 2021 (Figure 7). KMA ASOS-derived PM-ET ( $\text{mm day}^{-1}$ ) ranged from 0.28 to 14.41, and GK2A/AMI-derived PET ( $\text{mm day}^{-1}$ ) ranged from 0.00 to 11.10. In comparison with PM-ET derived from KMA ASOS stations, the total number of matchup data was 15,414, and GK2A/AMI-derived PET showed accuracy ( $\text{mm day}^{-1}$ ) of 0.649 (RMSE), 0.488 (MAE), 0.636 (STD), and  $-0.134$  (bias) with nRMSE of 0.168, indicating the MLP model tended to underestimate relative to the in-situ PM-ET overall. In particular, at PET values less than  $2.0 \text{ mm day}^{-1}$ , the tendency of underestimation of the MLP model was remarkable. Although the MLP model shows the tendency to underestimate, its underestimation was slight overall and it shows good performance estimating PM-ET from the KMA ASOS stations; Pearson's  $R$  was 0.954, and IOA was 0.975.

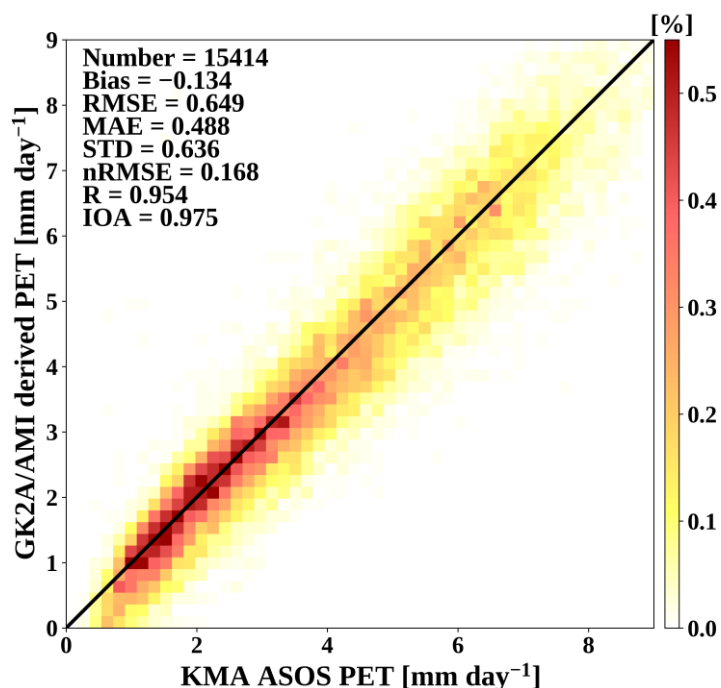


**Figure 7.** Comparison between GK2A/AMI satellite-derived PET estimates and PM-ET from ASOS stations operated by KMA, for the period 25 July 2020 to 31 July 2021. The color represents the proportion of the data relative to the total number of matchups.

From 25 July 2020 to 31 July 2021, we verified the accuracy of PET derived from GK2A/AMI by comparing them with the PM-ET from the KMA ASOS stations (Figure 8). RMSE ( $\text{mm day}^{-1}$ ) ranged from 0.449 (at station 136) to 0.871 (at station 185), nRMSE ranged from 0.117 (at station 159) to 0.237 (at station 169), and STD ( $\text{mm day}^{-1}$ ) ranged from 0.449 (at station 136) to 0.861 (at station 185) (Figure 8a–c). Bias ( $\text{mm day}^{-1}$ ) ranged from  $-0.568$  (at station 172) to 0.215 (at station 108) (Figure 8d). Pearson's  $R$  ranged from 0.891 (at station 181) to 0.979 (at station 136), and IOA ranged from 0.939 (at station 185) to 0.988 (at station 136). Overall, the PET estimated from GK2A/AMI using the MLP model were accurate relative to the PM-ET from KMA ASSOS stations (Figure 8e,f).

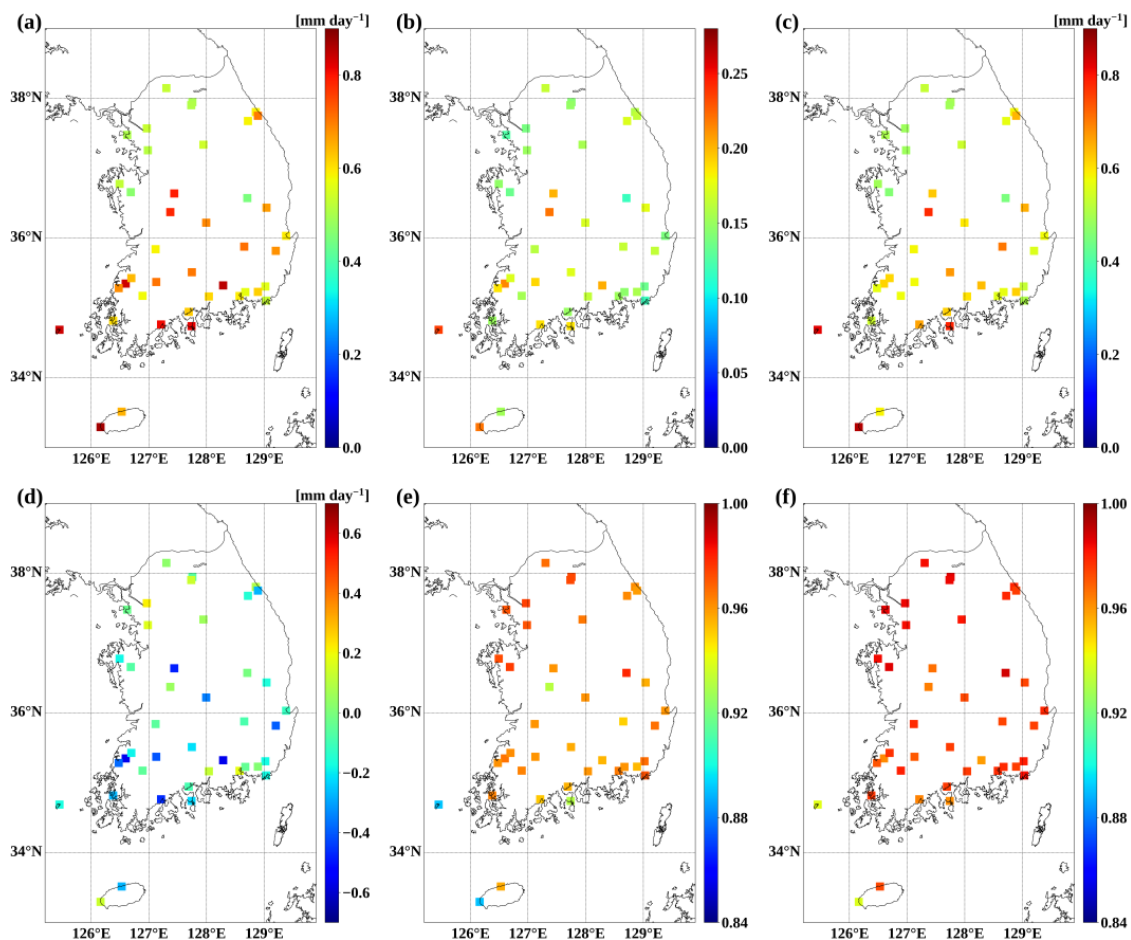


**Figure 8.** Spatial representation of the comparison between GK2A/AMI satellite-derived PET, and PET from ASOS stations operated by KMA, for the period 25 July 2020 to 31 July 2021. Accuracy is represented by (a) RMSE, (b) nRMSE, (c) STD, (d) bias, (e) Pearson's  $R$ , and (f) IOA.

We examined the seasonal characteristics of GK2A/AMI-derived PET. We simply classified the seasons into two classes; we hereafter referred to the period when monthly mean value of observed PET was less than  $3 \text{ mm day}^{-1}$  as cold seasons (November to February), and the period when monthly mean value of observed PET was more than  $3 \text{ mm day}^{-1}$  as warm seasons (March to October). In the cold seasons, KMA ASOS-derived PM-ET and GK2A/AMI-estimated PET both had lower values than in the warm seasons (Table 4). In cold seasons, RMSE ( $\text{mm day}^{-1}$ ) ranged from 0.399 to 0.671, Pearson's  $R$  ranged from 0.881 to 0.908, and nRMSE ranged from 0.193 to 0.244 (Table 5). On the other hand, in warm seasons, RMSE ( $\text{mm day}^{-1}$ ) ranged from 0.585 to 0.804, Pearson's  $R$  ranged from 0.901 to 0.960, and nRMSE ranged from 0.116 to 0.207. Regardless of seasons, the model was found to show low RMSE less than  $0.81 \text{ mm day}^{-1}$  and high Pearson's  $R$  more than 0.88, indicating that the model simulates the in-situ PET with high accuracy.

When compared to the warm seasons, the cold seasons show good performance in terms of RMSE, MAE, and STD, but poor performance in terms of nRMSE, Pearson's  $R$ , and IOA. These seasonal differences are caused by the seasonal variation of PET. As shown in Table 4, the lower the temperature, the lower the water vapor evaporated from soil and transpired by vegetation; the variation of PET in the warm seasons is higher than in the cold seasons [64,65]. Therefore, the low variation of PET in the cold seasons causes low RMSE, MAE, and STD; however, due to the small magnitude of PET in cold seasons, even a small error substantially affects the ratio-dependent accuracy score such as nRMSE, Pearson's  $R$ , and IOA.

**Table 4.** Comparison of observed PET and GK2A/AMI satellite-derived PET estimates.

Month	Observed PET (mm day <sup>-1</sup> )			Estimated PET (mm day <sup>-1</sup> )		
	Minimum	Maximum	Mean	Minimum	Maximum	Mean
August 2020	0.52	9.74	4.29	0.18	8.32	4.09
September 2020	0.69	8.66	3.78	0.00	8.25	3.27
October 2020	0.79	9.44	3.90	0.00	7.88	3.37
November 2020	0.39	6.96	2.76	0.00	5.98	2.52
December 2020	0.34	5.06	2.06	0.06	4.47	2.09
January 2021	0.30	6.52	1.87	0.00	4.76	1.84
February 2021	0.50	10.16	2.97	0.00	7.61	2.83
March 2021	0.28	9.04	3.67	0.08	8.72	3.59
April 2021	0.66	12.28	5.44	0.42	10.59	5.48
May 2021	0.54	14.41	5.14	0.65	11.10	5.27
June 2021	0.40	11.30	5.25	0.94	10.32	5.32
July 2021	0.52	10.22	5.50	0.92	9.47	5.31

**Table 5.** Accuracy (in terms of bias, RMSE, MAE, STD, nRMSE, R, and IOA), of the GK2A/AMI satellite-derived estimated PET, with respect to the month.

Month	No.	Bias (mm day <sup>-1</sup> )	RMSE (mm day <sup>-1</sup> )	MAE (mm day <sup>-1</sup> )	STD (mm day <sup>-1</sup> )	nRMSE	R	IOA
August 2020	1260	−0.208	0.671	0.510	0.638	0.156	0.949	0.968
September 2020	1234	−0.506	0.782	0.645	0.597	0.207	0.931	0.940
October 2020	1286	−0.529	0.804	0.651	0.605	0.206	0.901	0.913
November 2020	1241	−0.237	0.575	0.446	0.524	0.208	0.908	0.941
December 2020	1289	0.027	0.399	0.304	0.398	0.193	0.881	0.937
January 2021	1291	−0.028	0.456	0.353	0.455	0.244	0.883	0.932
February 2021	1170	−0.142	0.671	0.466	0.625	0.216	0.885	0.936
March 2021	1294	−0.073	0.585	0.448	0.581	0.160	0.954	0.974
April 2021	1250	0.035	0.763	0.582	0.762	0.140	0.928	0.963
May 2021	1293	0.131	0.704	0.512	0.692	0.137	0.960	0.979
June 2021	1249	0.067	0.609	0.457	0.605	0.116	0.955	0.977
July 2021	1275	−0.186	0.710	0.530	0.685	0.129	0.940	0.965

## 4. Discussions

### 4.1. NIFoS Flux Towers

Because the ANN-based daily ET model was trained using the PM-ET data from the KMA ASOS stations, we examined the availability of the GK2A/AMI-derived PET by comparing it with EC-ET data. We compared daily PET derived from GK2A/AMI for the Korean Peninsula with EC-ET derived from NIFoS flux tower, for the period 25 July 2020 to 31 July 2021 (Figure 9). NIFoS flux tower-derived EC-ET (mm day<sup>-1</sup>) ranged from 0.02 to 9.82, and GK2A/AMI-derived PET (mm day<sup>-1</sup>) ranged from 0.00 to 10.06. In comparison with EC-ET derived from NIFoS flux tower, the total number of matchup data was 654, and GK2A/AMI-derived PET showed the accuracy (mm day<sup>-1</sup>) of 1.730 (RMSE), 1.409 (MAE), 1.235 (STD), and 1.212 (bias) with nRMSE of 0.525, indicating the PET derived from GK2A/AMI using the MLP model tended to overestimate relative to the EC-ET derived from NIFoS flux tower overall. The model performed in following the trend in the EC-ET data; Pearson's *R* was 0.809, and IOA was 0.822.

In theoretical conditions, the PET derived from the PM method was not expected to match with the AET derived from the EC method. Although the differences depend on the environmental conditions and PET retrieval methods, the PM method generally overestimated ET compared with EC-ET in both hourly and daily time scales [47]. However, the comparison result shows a high correlation with both variables and between the input parameters for both variables, which indicates that PM-ET and EC-ET are affected by the same factors [66,67]. Because the PM method quantifies water vapor loss in sufficient soil

moisture conditions, it overestimates ET relative to EC-ET under the dry conditions [67]. However, in sufficient soil moisture conditions on rainy days, the PM method nonetheless overestimated ET relative to EC-ET [49,68]. Furthermore, the differences between PM-ET and EC-ET depend on the environmental conditions, the tendency to overestimate ET was strong with intense net radiation and water vapor deficit [67,69]. Another possible reason for the overestimation is that PM-ET does not consider the complicated structure of the forest. The comparison result between PM-ET and EC-ET depended on the reference level, and the accuracy of PM-ET increased with the reference level of measurement [47]. The PM method assumes that the vegetation is a single big leaf, and ET occurs on a surface with zero plane displacement. However, vegetation conditions vary depending on the spatiotemporal environment, and ET occurs in the forest floor to the top of vegetation. On the other hand, during the vegetation growing season with low leaf area index, surface and underground ET take a substantial part of the water vapor cycle. Because of that, PM-ET could underestimate ET at a small leaf area index, compared with EC-ET [47]. Another possible reason for overestimation is that the PM method cannot accurately include the resistance due to the surface canopy or soil conditions [69]. Since PM-ET data depend highly on surface conductance; its overestimation could cause the overestimation of ET [47,70]. Although the PM model overestimated ET, it showed a high correlation with the EC-ET data. Since the model accounts for radiative and aerodynamic conditions, it might produce more reliable estimates of AET than other PET models [71].

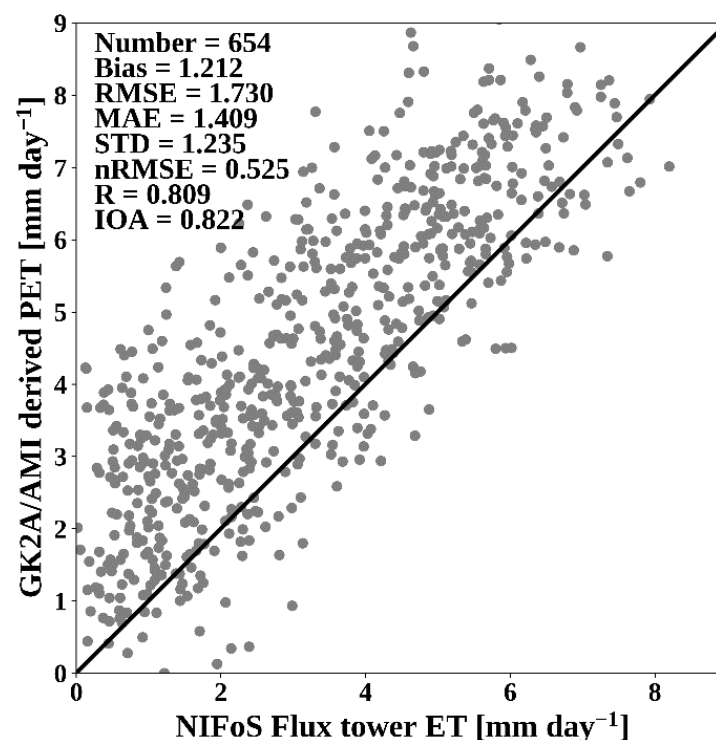


**Figure 9.** Comparison between GK2A/AMI satellite-derived and NIFoS flux tower-derived ET from 25 July 2020 to 31 July 2021.

#### 4.2. Comparison with MODIS

To validate the GK2A/AMI-derived daily PET data, we compared it with the Terra/MODIS PET product. Because Terra/MODIS produces an 8-days PET composite, we produced 8-days aggregates of daily PET data from the GK2A/AMI satellite and from the KMA ASOS stations. In the KMA ASOS stations, when the number of daily PET data for 8-days was less than 8, it was excluded from the validation data. We then compared the Terra/MODIS PET data with the KMA ASOS station and GK2A/AMI satellite PET data, for the period 27 July 2020 to 27 July 2021 (Figure 10).

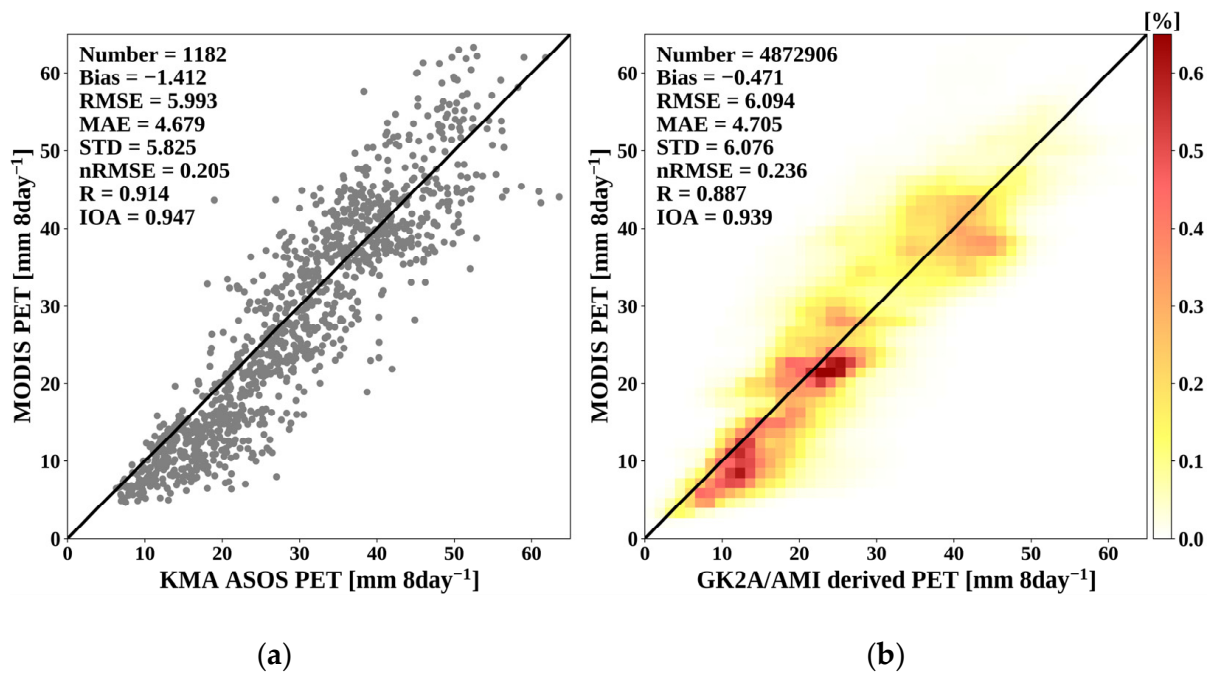


**Figure 10.** Validation of Terra/MODIS PET data for the period 27 July 2020 to 27 July 2021, relative to PET from (a) ASOS stations operated by KMA, and (b) the GK2A/AMI satellite.

In comparison with the KMA ASOS station PET data, the Terra/MODIS PET data showed accuracy (mm 8 day<sup>-1</sup>) of 5.993 (RMSE), 4.679 (MAE), 5.825 (STD), and -1.412 (bias) with an nRMSE of 0.205; Pearson's *R* was 0.914 and IOA was 0.947, indicating the Terra/MODIS PET data tended to underestimate PET relative to KMA ASOS (Figure 10a). The underestimation of the Terra/MODIS PET data was remarkably shown in the PET of less than 20 mm 8 day<sup>-1</sup>. In previous studies, the MODIS-based PET product was converted to daily PET and compared with PM-ET. The assessment of MODIS-based PET product varied on the land cover and showed Pearson's *R* of 0.71 to 0.94 [72,73]. Although the previous studies and this study used the verification with a daily and 8-day product, respectively, the high Pearson's *R* means that MODIS-based PET product is useful for ET monitoring on the Korean Peninsula. In comparison with the GK2A/AMI-derived PET data, the Terra/MODIS PET data showed accuracy (mm 8 day<sup>-1</sup>) of 6.094 (RMSE), 4.705 (MAE), 6.076 (STD), and -0.471 (bias) with an nRMSE of 0.236; Pearson's *R* was 0.887 and IOA was 0.939, indicating the Terra/MODIS PET data tended to underestimate PET relative to GK2A/AMI (Figure 10b). The underestimation of the Terra/MODIS PET data was remarkably shown in the PET of less than 20 mm 8 day<sup>-1</sup>, indicating the comparing result of GK2A was consistent with that of KMA ASOS.

For the assessment of the spatial distribution of GK2A/AMI-derived PET, we verified the accuracy of Terra/MODIS PET relative to the PET data for each KMA ASOS station and GK2A/AMI coordinate for the period 27 July 2020 to 27 July 2021 (Figure 11). In comparison with the KMA ASOS station data, RMSE (mm 8 day<sup>-1</sup>) ranged from 3.056 (at station 119) to 10.061 (at station 105); bias (mm 8 day<sup>-1</sup>) ranged from -5.692 (at station 105) to 1.075 (at station 177); and Pearson's *R* ranged from 0.748 (at station 185) to 0.981 (at station 119) (Figure 11a–c). Relative to the GK2A/AMI-derived PET, RMSE (mm 8 day<sup>-1</sup>) ranged from 1.445 to 17.039, bias (mm 8 day<sup>-1</sup>) from -14.549 to 13.627, and Pearson's *R* from 0.305 to 0.991 (Figure 11d–f). In Terra/MODIS PET, the result compared with KMA ASOS PET (Figure 11a–c) was consistent with that of GK2A/AMI-PET (Figure 11d–f). In particular, in the eastern region of the Korean Peninsula, it showed high RMSE, negative bias, and low Pearson's *R* compared with the other area in the Korean Peninsula.

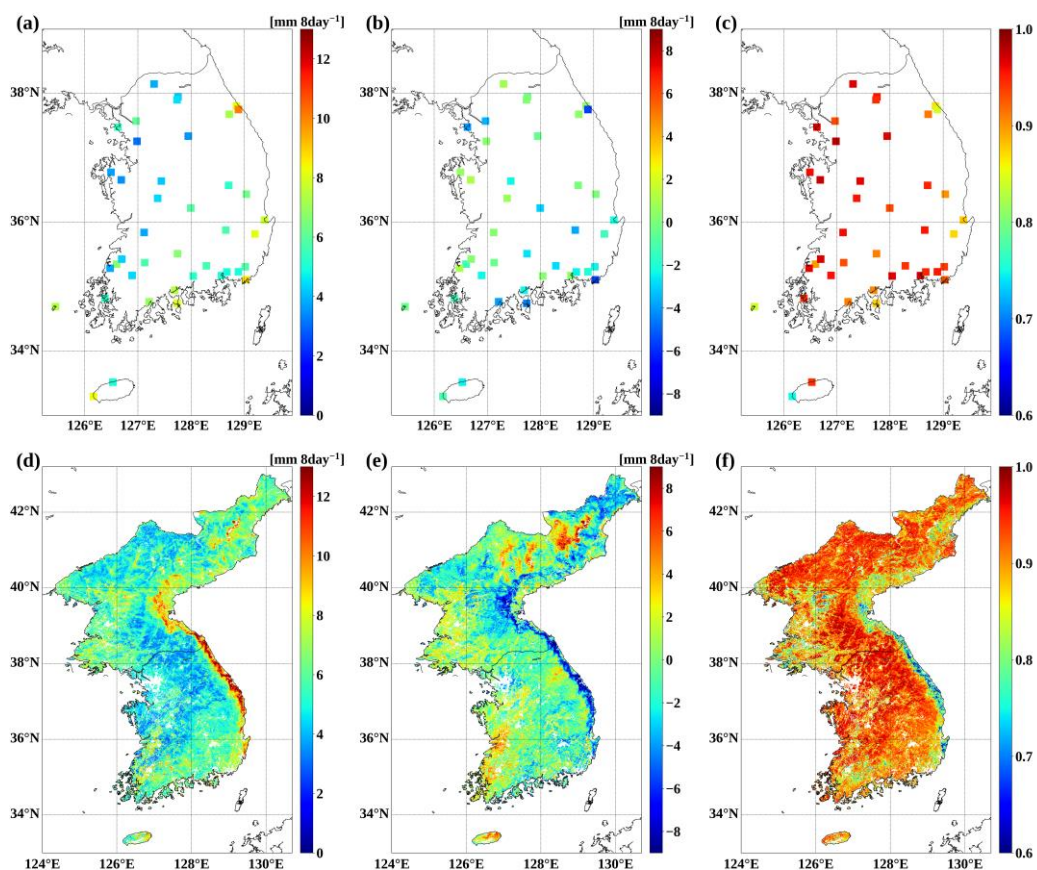


**Figure 11.** Accuracy of Terra/MODIS PET for the period 27 July 2020 to 27 July 2021 at (a–c) the ASOS stations operated by KMA, and (d–f) the coordinates of the GK2A/AMI satellite. The accuracy is represented by (a,d) RMSE, (b,e) bias, and (c,f) Pearson's  $R$ .

The KMA ASOS station-derived PM-ET data showed a Pearson correlation of 0.914 with Terra/MODIS PET (Figure 10a), and 0.954 with GK2A/AMI-derived PET (Figure 7). While the Terra/MODIS PET algorithm is optimized for global coverage, our MLP model was locally optimized for the Korean Peninsula. Furthermore, since our MLP model used daily remotely sensed and numerical model product not related to cloud, the GK2A-derived PET shows fine temporal resolution and has no masked value due to cloud relative to Terra/MODIS product. Therefore, the GK2A/AMI-derived PET performed better than Terra/MODIS for estimating PET on the Korean Peninsula. Relative to the GK2A/AMI-derived PET and in-situ PM-ET data, the consistency of the Terra/MODIS PET data decreased remarkably for the eastern region of the Korean Peninsula (Figure 11). In the eastern coastal area of the Korean Peninsula, elevation decreases dramatically (Figure 2). In contrast to the lack of consistency with the Terra/MODIS PET data, the GK2A/AMI-derived PET and in-situ PM-ET were highly correlated (Pearson's  $R > 0.879$ ), regardless of the topography (Figure 8). This result indicates that Terra/MODIS did not reflect the local terrain characteristics of the Korean Peninsula, due to its global optimization. Thus, for ET monitoring with high spatiotemporal variability on the Korean Peninsula, the real-time daily GK2A/AMI-derived PET was more suitable (due to local optimization) than the 8-days Terra/MODIS PET product.

#### 4.3. Previous Studies on the Korean Peninsula

The Korean Peninsula comprises various vegetation cover types and shows specific agrometeorological characteristics, and it is able to perform agrometeorological analysis using ET data. When investigating the ensemble model of virtual water content based on ET, it was found that the ensemble virtual water content and production of rice and maize

decreased in future projections, which affected future water consumption on the Korean Peninsula [74]. Birhanu et al. [75], when constructing hydrological models, investigated the effect of model complexity and ET calculation methods on model performance based on the in-situ measurement. Um et al. [76] estimated the spatial distribution of ET based on in-situ measurements using the hybrid Kriging method and revealed various ET characteristics depending on the distance from the coast and elevation level above the ground surface. Jung et al. [77] developed the physiological modules to simulate the canopy photosynthesis and ET process and established the relationship of photosynthesis and ET with crop production based on satellite data and in-situ measurements. Similar to this study, Kim et al. [41] developed the ML model estimating daily PET for the Korean Peninsula using satellite data and NWP data. MODIS-based monthly vegetation index data, multi-microwave satellite-derived precipitation data, and LDAPS data were used as input data of the random forest model. The model showed accuracy ( $\text{mm day}^{-1}$ ) of 1.038 (RMSE), 0.790 (MAE), and 0.007 (bias) with Pearson's  $R$  of 0.870. The model developed in this study not only has better accuracy but also has the advantage of retrieval in real-time.

## 5. Conclusions

This paper presents an ANN model that retrieves daily PET in real-time for the Korean Peninsula, using GK2A/AMI-derived data, microwave composite data, and NWP data. We used the data from 25 July 2019 to 24 July 2020 for model training, and 25 July 2020, to 31 July 2021 for model testing. In comparison with the KMA ASOS station-derived PM-ET, the ANN-based GK2A-derived PET showed high accuracy ( $\text{mm day}^{-1}$ ) of 0.649 (RMSE) and  $-0.134$  (bias); Pearson's  $R$  of 0.954; and IOA of 0.975. In validating the spatial distribution, the ANN model-estimated daily PET showed high accuracy at all KMA ASOS stations. To assess the efficiency of the GK2A/AMI-derived PET, we verified it using NIFoS flux tower-derived EC-ET, which showed that GK2A/AMI-derived PET overestimated ET. Furthermore, we assessed the performance of our ANN model by comparing it with operational Terra/MODIS PET products with 8-days temporal resolution. Because it was locally optimized, our ANN model outperformed Terra/MODIS PET over the Korean Peninsula. GK2A/AMI-derived PET performed particularly better than the Terra/MODIS PET product for the eastern coastal region of the Korean Peninsula, where elevation changes dramatically.

Although GK2A/AMI-derived PET showed high accuracy, it is necessary to extend its spatial coverage for overcoming its local optimization. When applying the additional in-situ measurements on other areas to the model, it is possible to improve the model in terms of spatial coverage. Furthermore, in order to develop the model estimating ET, we used and optimized the MLP model, but it is able to apply diverse ANN methods such as recurrent neural network, convolutional neural network, and long short-term memory. When applying and validating various ANN methods, it is possible to improve the accuracy of the model estimating ET.

ET is a key indicator to investigate the effects of the meteorological drought on vegetation activities. GK2A/AMI-derived 2-dimensional ET is thought to be a useful tool in examining the drought affecting the Korean Peninsula. In further studies, we will attempt to investigate drought on the Korean Peninsula by examining the relationship of GK2A/AMI-derived ET and precipitation data with vegetation information. This study contributes to understanding air-land interactions, and the development of ANN approaches using satellite and NWP data.

**Author Contributions:** Conceptualization, J.-C.J.; methodology, validation, and writing—original draft preparation, J.-C.J.; writing—review and editing, E.-H.S., K.-H.P. and S.L. All authors have read and agreed to the published version of the manuscript.

**Funding:** This work was funded by the Korea Meteorological Administration's Research and Development Program "Technical Development on Weather Forecast Support and Convergence Service using Meteorological Satellites" under Grant (KMA2020-00120).

**Institutional Review Board Statement:** Not applicable.

**Informed Consent Statement:** Not applicable.

**Data Availability Statement:** GK-2A/AMI data used in this study are available on <http://datasvc.nmsc.kma.go.kr/datasvc/html/main/main.do?lang=en> (accessed on 13 July 2021). In-situ data from KMA ASOS stations and NIFoS flux towers used in this study are available on <https://data.kma.go.kr/cmmn/main.do> and <http://know.nifos.go.kr/know/service/flux/fluxIntro.do>, respectively (accessed on 13 July 2021).

**Conflicts of Interest:** The authors declare no conflict of interest.

## Abbreviations

ADAM	A Method for Stochastic Optimization
AET	Actual Evapotranspiration
AMI	Advanced Meteorological Imager
ANN	Artificial Neural Networks
ASR	Absorbed Shortwave Radiation
BN	Batch Normalization
COMS	Communication, Ocean and Meteorological Satellite
DEM	Digital Elevation Model
DLR	Downward Longwave Radiation
DSR	Downward Shortwave Radiation
EC	Eddy Covariance
ELU	Exponential Linear Unit
ESR	Extraterrestrial Solar Radiation
ET	Evapotranspiration
FAO	Food and Agriculture Organization of the United Nations
GEO	Geostationary Orbit
GK2A	GEOstationary Korea Multi-Purpose SATellite 2A
IMERG	Integrated Multi-satellitE Retrievals for Global Precipitation Measurement
KMA	Korea Meteorological Administration
LDAPS	Local Data Assimilation and Prediction System
LEO	Low Earth Orbit
MDA	Mean Decrease Accuracy
ML	Machine Learning
MLP	Multilayer Perceptron
MODIS	Moderate Resolution Imaging Spectroradiometer
NDVI	Normalized Difference Vegetation Index
NIFoS	National Institute of Forest Science
NMSC	National Meteorological Satellite Center
NWP	Numerical Weather Prediction
OLR	Outgoing Longwave Radiation
PET	Potential Evapotranspiration
PM	Penman-Monteith
RSR	Reflected Shortwave Radiation
SPI6	Standardized Precipitation Index for Six Months
SRTM	Shuttle Radar Topography Mission
ULR	Upward Longwave Radiation
UM	Unified Model

## References

1. Zhao, L.L.; Xia, J.; Xu, C.Y.; Wang, Z.G.; Sobkowiak, L.; Long, C. Evapotranspiration estimated methods in hydrological simulation. *J. Geogr. Sci.* **2013**, *23*, 359–369. [[CrossRef](#)]
2. Fan, Z.; Thomas, A. Decadal changes of reference crop evapotranspiration attribution: Spatial and temporal variability over China 1960–2011. *J. Hydrol.* **2018**, *560*, 461–470. [[CrossRef](#)]
3. Pilgrim, D.H.; Chapman, R.G.; Doran, D.G. Problems of rainfall-runoff modelling in arid and semiarid regions. *Hydrol. Sci. J.* **1988**, *33*, 379–400. [[CrossRef](#)]

4. Iglesias, A.; Garrote, L. Adaptation strategies for agricultural water management under climate change in Europe. *Agric. Water Manag.* **2015**, *155*, 113–124. [[CrossRef](#)]
5. Vicente-Serrano, S.M.; Beguería, S.; López-Moreno, J.I. A multiscalar drought index sensitive to global warming: The standardized precipitation evapotranspiration index. *J. Clim.* **2010**, *23*, 1696–1718. [[CrossRef](#)]
6. Tian, L.; Leason, Z.T.; Quiring, S.M. Developing a hybrid drought index: Precipitation Evapotranspiration Difference Condition Index. *Clim. Risk Manag.* **2020**, *29*, 100238. [[CrossRef](#)]
7. Tsakiris, G.; Vangelis, H. Establishing a drought index incorporating evapotranspiration. *Eur. Water* **2005**, *9*, 3–11.
8. Elbeltagi, A.; Kumari, N.; Dharpure, J.K.; Mokhtar, A.; Alsafadi, K.; Kumar, M.; Mehdinejadiani, B.; Ramezani Etedali, H.; Brouziyne, Y.; Towfiqul Islam, A.R.M.; et al. Prediction of Combined Terrestrial Evapotranspiration Index (CTEI) over Large River Basin Based on Machine Learning Approaches. *Water* **2021**, *13*, 547. [[CrossRef](#)]
9. Tadese, M.; Kumar, L.; Koech, R. Long-term variability in potential evapotranspiration, water availability and drought under climate change scenarios in the Awash River Basin, Ethiopia. *Atmosphere* **2020**, *11*, 883. [[CrossRef](#)]
10. Avanzi, F.; Rungee, J.; Maurer, T.; Bales, R.; Ma, Q.; Glaser, S.; Conklin, M. Climate elasticity of evapotranspiration shifts the water balance of Mediterranean climates during multi-year droughts. *Hydrol. Earth Syst. Sci.* **2020**, *24*, 4317–4337. [[CrossRef](#)]
11. Liu, C.; Yang, C.; Yang, Q.; Wang, J. Spatiotemporal drought analysis by the standardized precipitation index (SPI) and standardized precipitation evapotranspiration index (SPEI) in Sichuan Province, China. *Sci. Rep.* **2021**, *11*, 1280. [[CrossRef](#)]
12. Abdelmalek, M.B.; Nouiri, I. Study of trends and mapping of drought events in Tunisia and their impacts on agricultural production. *Sci. Total Environ.* **2020**, *734*, 139311. [[CrossRef](#)]
13. Yao, N.; Li, Y.; Dong, Q.G.; Li, L.; Peng, L.; Feng, H. Influence of the accuracy of reference crop evapotranspiration on drought monitoring using standardized precipitation evapotranspiration index in mainland China. *Land Degrad. Dev.* **2020**, *31*, 266–282. [[CrossRef](#)]
14. Allen, R.G.; Fisher, D.K. Low-Cost Electronic Weighing Lysimeters. *Trans. ASAE* **1990**, *33*, 1823–1833. [[CrossRef](#)]
15. Xu, C.Y.; Chen, D. Comparison of seven models for estimation of evapotranspiration and groundwater recharge using lysimeter measurement data in Germany. *Hydrol. Process.* **2005**, *19*, 3717–3734. [[CrossRef](#)]
16. Srivastava, A.; Sahoo, B.; Raghuvanshi, N.S.; Singh, R. Evaluation of Variable-Infiltration Capacity Model and MODIS-Terra Satellite-Derived Grid-Scale Evapotranspiration Estimates in a River Basin with Tropical Monsoon-Type Climatology. *J. Irrig. Drain. Eng.* **2017**, *143*, 04017028. [[CrossRef](#)]
17. Penman, H.L. Natural evaporation from open water, bare soil and grass. *Proc. R. Soc. Lond. A* **1948**, *194*, 120–145.
18. Monteith, J.L. Evaporation and environment. *Symp. Soc. Exp. Biol.* **1965**, *19*, 205–224. [[PubMed](#)]
19. Priestley, C.H.B.; Taylor, R.J. On the assessment of surface heat flux and evaporation using large scale parameters. *Mon. Weather Rev.* **1972**, *100*, 81–92. [[CrossRef](#)]
20. Hargreaves, G.H.; Samani, Z.A. Reference crop evapotranspiration from temperature. *Appl. Eng. Agric.* **1985**, *1*, 96–99. [[CrossRef](#)]
21. Allen, R.G.; Pereira, L.S.; Raes, D.; Smith, M. *Crop Evapotranspiration: Guidelines for Computing Crop Water Requirements*; Food and Agriculture Organization of the United Nations: Rome, Italy, 1998.
22. Allen, R.G.; Smith, M.; Perrier, A.; Pereira, L.S. An update for the definition of reference evapotranspiration. *ICID Bull.* **1994**, *43*, 1–34.
23. Wilby, R.L.; Yu, D. Rainfall and temperature estimation for a data sparse region. *Hydrol. Earth Syst. Sci.* **2013**, *17*, 3937–3955. [[CrossRef](#)]
24. Courault, D.; Seguin, B.; Olioso, A. Review on estimation of evapotranspiration from remote sensing data: From empirical to numerical modeling approaches. *Irrig. Drain. Syst.* **2005**, *19*, 223–249. [[CrossRef](#)]
25. Mu, Q.; Heinsch, F.A.; Zhao, M.; Running, S.W. Development of a global evapotranspiration algorithm based on MODIS and global meteorology data. *Remote Sens. Environ.* **2007**, *111*, 519–536. [[CrossRef](#)]
26. McCabe, M.F.; Wood, E.F. Scale influences on the remote estimation of evapotranspiration using multiple satellite sensors. *Remote Sens. Environ.* **2006**, *105*, 271–285. [[CrossRef](#)]
27. Long, D.; Longuevergne, L.; Scanlon, B.R. Uncertainty in evapotranspiration from land surface modeling, remote sensing, and GRACE satellites. *Water Resour. Res.* **2014**, *50*, 1131–1151. [[CrossRef](#)]
28. Gomis-Cebolla, J.; Jimenez, J.C.; Sobrino, J.A.; Corbari, C.; Mancini, M. Intercomparison of remote-sensing based evapotranspiration algorithms over amazonian forests. *Int. J. Appl. Earth Obs. Geoinf.* **2019**, *80*, 280–294. [[CrossRef](#)]
29. Chia, M.Y.; Huang, Y.F.; Koo, C.H.; Fung, K.F. Recent advances in evapotranspiration estimation using artificial intelligence approaches with a focus on hybridization techniques—A Review. *Agron. Basel* **2020**, *10*, 101. [[CrossRef](#)]
30. Zhang, L.; Lemeur, R. Evaluation of daily evapotranspiration estimates from instantaneous measurements. *Agric. For. Meteorol.* **1995**, *74*, 139–154. [[CrossRef](#)]
31. Bae, H.; Ji, H.; Lim, Y.-J.; Ryu, Y.; Kim, M.-H.; Kim, B.-J. Characteristics of drought propagation in South Korea: Relationship between meteorological, agricultural, and hydrological droughts. *Nat. Hazards* **2019**, *99*, 1–16. [[CrossRef](#)]
32. Azam, M.; Maeng, S.; Kim, H.; Lee, S.; Lee, J. Spatial and Temporal Trend Analysis of Precipitation and Drought in South Korea. *Water* **2018**, *10*, 765. [[CrossRef](#)]
33. Jang, K.; Kang, S.; Lim, Y.; Jeong, S.; Kim, J.; Kimball, J.S.; Hong, S.Y. Monitoring daily evapotranspiration in Northeast Asia using MODIS and a regional Land Data Assimilation System. *J. Geophys. Res. Atmos.* **2013**, *118*, 927–940. [[CrossRef](#)]

34. Yang, F.; White, M.A.; Michaelis, A.R.; Ichii, K.; Hashimoto, H.; Votava, P.; Zhu, A.-X.; Nemani, R.R. Prediction of continental-scale evapotranspiration by combining MODIS and AmeriFlux data through support vector machine. *IEEE Trans. Geosci. Remote Sens.* **2006**, *44*, 3452–3461. [[CrossRef](#)]
35. Yuan, W.; Liu, S.; Yu, G.; Bonnefond, J.-M.; Chen, J.; Davis, K.; Desai, A.R.; Goldstein, A.H.; Gianelle, D.; Rossi, F.; et al. Global estimates of evapotranspiration and gross primary production based on MODIS and global meteorology data. *Remote Sens. Environ.* **2010**, *114*, 1416–1431. [[CrossRef](#)]
36. Fan, J.; Yue, W.; Wu, L.; Zhang, F.; Cai, H.; Wang, X.; Lu, X.; Xiang, Y. Evaluation of SVM, ELM and four tree-based ensemble models for predicting daily reference evapotranspiration using limited meteorological data in different climates of China. *Agric. For. Meteorol.* **2018**, *263*, 225–241. [[CrossRef](#)]
37. Granata, F.; Gargano, R.; de Marinis, G. Artificial intelligence-based approaches to evaluate actual evapotranspiration in wetlands. *Sci. Total Environ.* **2020**, *703*, 135653. [[CrossRef](#)]
38. Rashid Niaghi, A.; Hassanijalilian, O.; Shiri, J. Estimation of reference evapotranspiration using spatial and temporal machine learning approaches. *Hydrology* **2021**, *8*, 25. [[CrossRef](#)]
39. Torres, A.F.; Walker, W.R.; McKee, M. Forecasting daily potential evapotranspiration using machine learning and limited climatic data. *Agric. Water Manag.* **2011**, *98*, 553–562. [[CrossRef](#)]
40. Käfer, P.S.; da Rocha, N.S.; Diaz, L.R.; Kaiser, E.A.; Santos, D.C.; Veeck, G.P.; Robérti, D.R.; Rolim, S.B.A.; Oliveira, G.G. Artificial neural networks model based on remote sensing to retrieve evapotranspiration over the Brazilian Pampa. *J. Appl. Remote Sens.* **2020**, *14*, 038504. [[CrossRef](#)]
41. Kim, N.; Kim, K.; Lee, S.; Cho, J.; Lee, Y. Retrieval of daily reference evapotranspiration for croplands in South Korea using machine learning with satellite images and numerical weather prediction data. *Remote Sens.* **2020**, *12*, 3642. [[CrossRef](#)]
42. Cui, Y.; Song, L.; Fan, W. Generation of spatio-temporally continuous evapotranspiration and its components by coupling a two-source energy balance model and a deep neural network over the Heihe River Basin. *J. Hydrol.* **2021**, *597*, 126176. [[CrossRef](#)]
43. Jang, J.C.; Lee, S.; Sohn, E.H.; Noh, Y.J.; Miller, S.D. Combined dust detection algorithm for Asian Dust events over East Asia using GK2A/AMI: A case study in October 2019. *Asia Pac. J. Atmos. Sci.* **2021**, 1–20. [[CrossRef](#)]
44. Huffman, G.; Bolvin, D.; Braithwaite, D.; Hsu, K.; Joyce, R.; Xie, P. *NASA Global Precipitation Measurement (GPM) Integrated Multi-Satellite Retrievals for GPM (IMERG)*; Algorithm Theoretical Basis Document, Version 4.4; NASA: Greenbelt, MD, USA, 2014; p. 30.
45. Song, H.J.; Lim, B.; Joo, S. Evaluation of rainfall forecasts with heavy rain types in the high-resolution unified model over South Korea. *Weather Forecast.* **2019**, *34*, 1277–1293. [[CrossRef](#)]
46. Rabus, B.; Eineder, M.; Roth, A.; Bamler, R. The shuttle radar topography mission—A new class of digital elevation models acquired by spaceborne radar. *ISPRS J. Photogramm. Eng. Remote Sens.* **2003**, *57*, 241–262. [[CrossRef](#)]
47. Shi, T.T.; Guan, D.X.; Wu, J.B.; Wang, A.Z.; Jin, C.J.; Han, S.J. Comparison of methods for estimating evapotranspiration rate of dry forest canopy: Eddy covariance, Bowen ratio energy balance, and Penman-Monteith equation. *J. Geophys. Res.* **2008**, *113*, D19116. [[CrossRef](#)]
48. Duffie, J.A.; Beckman, W.A. *Solar Engineering of Thermal Process.*; John Wiley and Sons: New York, NY, USA, 1991.
49. Tayfur, G. Artificial neural networks for sheet sediment transport. *Hydrol. Sci. J.* **2002**, *47*, 879–892. [[CrossRef](#)]
50. Tayfur, G.; Singh, V.P. ANN and fuzzy logic models for simulating event-based Rainfall-Runoff. *J. Hydraul. Eng.* **2006**, *132*, 1321–1330. [[CrossRef](#)]
51. Dawson, C.; Wilby, R. An artificial neural network approach to rainfall-runoff modelling. *Int. Assoc. Sci. Hydrol. Bull.* **1998**, *43*, 47–66. [[CrossRef](#)]
52. Tamouridou, A.A.; Alexandridis, T.K.; Pantazi, X.E. Application of multilayer perceptron with automatic relevance determination on weed mapping using UAV multispectral imagery. *Sensors* **2017**, *17*, 2307. [[CrossRef](#)]
53. Zhang, B.; Zhang, M.; Kang, J.; Hong, D.; Xu, J.; Zhu, X. Estimation of PM<sub>x</sub> concentrations from Landsat 8 OLI images based on a multilayer perceptron neural network. *Remote Sens.* **2019**, *11*, 646. [[CrossRef](#)]
54. Jiang, W.; He, G.; Long, T.; Ni, Y.; Liu, H.; Peng, Y.; Lv, K.; Wang, G. Multilayer Perceptron Neural Network for Surface Water Extraction in Landsat 8 OLI Satellite Images. *Remote Sens.* **2018**, *10*, 755. [[CrossRef](#)]
55. Clevert, D.-A.; Unterthiner, T.; Hochreiter, S. Fast and Accurate Deep Network Learning by Exponential Linear Units (ELUs). *arXiv* **2015**, arXiv:151107289.
56. Ioffe, S.; Szegedy, C. Batch normalization: Accelerating deep network training by reducing internal covariate shift. In Proceedings of the International Conference on Machine Learning (ICML), Lille, France, 6–11 July 2015.
57. Chen, C.; Gong, W.; Chen, Y.; Li, W. Object detection in remote sensing images based on a scene-contextual feature pyramid network. *Remote Sens.* **2019**, *11*, 339. [[CrossRef](#)]
58. Kingma, D.P.; Ba, J. Adam: A method for stochastic optimization. *arXiv* **2014**, arXiv:1412.6980.
59. McCaffrey, D.R.; Hopkinson, C. Modeling Watershed-Scale Historic Change in the Alpine Treeline Ecotone Using Random Forest. *Can. J. Remote Sens.* **2020**, *46*, 715–732. [[CrossRef](#)]
60. Hupet, F.; Vanclooster, M. Effect of the sampling frequency of meteorological variables on the estimation of the reference evapotranspiration. *J. Hydrol.* **2001**, *243*, 192–204. [[CrossRef](#)]
61. Lang, D.; Zheng, J.; Shi, J.; Liao, F.; Ma, X.; Wang, W.; Chen, X.; Zhang, M. A comparative study of potential evapotranspiration estimation by eight methods with FAO Penman–Monteith method in southwestern China. *Water* **2017**, *9*, 734. [[CrossRef](#)]

62. Willmott, C.J.; Robeson, S.M.; Matsuura, K. A refined index of model performance. *Int. J. Climatol.* **2012**, *32*, 2088–2094. [[CrossRef](#)]
63. Mo, X.; Liu, S.; Lin, Z.; Wang, S.; Hu, S. Trends in land surface evapotranspiration across China with remotely sensed NDVI and climatological data for 1981–2010. *Hydrol. Sci. J.* **2015**, *60*, 2163–2177. [[CrossRef](#)]
64. Li, X.; Wang, L.; Chen, D.; Yang, K.; Wang, A. Seasonal evapotranspiration changes (1983–2006) of four large basins on the Tibetan Plateau. *J. Geophys. Res.* **2014**, *119*, 13079–13095. [[CrossRef](#)]
65. Li, M.; Chu, R.; Shen, S.; Islam, A.R.M.T. Quantifying climatic impact on reference evapotranspiration trends in the Huai River Basin of eastern China. *Water* **2018**, *10*, 144. [[CrossRef](#)]
66. Gharsallah, O.; Facchi, A.; Gandolfi, C. Comparison of six evapotranspiration models for a surface irrigated maize agro-ecosystem in Northern Italy. *Agric. Water Manag.* **2013**, *130*, 119–130. [[CrossRef](#)]
67. Fleischer, E.; Böltner, J.; Klemm, O. Summer evapotranspiration in western Siberia: A comparison between eddy covariance and Penman method formulations. *Hydrol. Process.* **2015**, *29*, 4498–4513. [[CrossRef](#)]
68. Anderson, R.G.; Wang, D.; Tirado-Corbalá, R.; Zhang, H.; Ayars, J.E. Divergence of reference evapotranspiration observations with windy tropical conditions. *Hydro. Earth Syst. Sci. Discuss.* **2014**, *11*, 6473–6518.
69. Gao, G.; Zhang, X.; Yu, T.; Liu, B. Comparison of three evapotranspiration models with eddy covariance measurements for a *Populus euphratica* Oliv. forest in an arid region of northwestern China. *J. Arid Land* **2016**, *8*, 146–156. [[CrossRef](#)]
70. Hughes, C.E.; Kalma, J.D.; Binning, P.; Willgoose, G.R.; Vertzonis, M. Estimating evapotranspiration for a temperate salt marsh Newcastle, Australia. *Hydrol. Process.* **2001**, *15*, 957–975. [[CrossRef](#)]
71. Li, S.; Kang, S.Z.; Zhang, L.; Zhang, J.H.; Du, T.S.; Tong, L.; Ding, R.S. Evaluation of six potential evapotranspiration models for estimating crop potential and actual evapotranspiration in arid regions. *J. Hydrol.* **2016**, *543*, 450–461. [[CrossRef](#)]
72. Sun, Z.; Wang, Q.; Ouyang, Z.; Watanabe, M.; Matsushita, B.; Fukushima, T. Evaluation of MOD16 algorithm using MODIS and ground observational data in winter wheat field in North China Plain. *Hydrol. Process.* **2007**, *21*, 1196–1206. [[CrossRef](#)]
73. Kim, J.Y.; Hogue, T.S. Evaluation of a MODIS-based potential evapotranspiration product at the point scale. *J. Hydrometeor.* **2008**, *9*, 444–460. [[CrossRef](#)]
74. Lim, C.-H.; Kim, S.H.; Choi, Y.; Kafatos, M.C.; Lee, W.-K. Estimation of the virtual water content of main crops on the Korean Peninsula using multiple regional climate models and evapotranspiration methods. *Sustainability* **2017**, *9*, 1172. [[CrossRef](#)]
75. Birhanu, D.; Kim, H.; Jang, C.; Park, S. Does the complexity of evapotranspiration and hydrological models enhance robustness? *Sustainability* **2018**, *10*, 2837. [[CrossRef](#)]
76. Um, M.J.; Kim, Y.; Park, D. Spatial and temporal variations in reference crop evapotranspiration in a Mountainous Island, Jeju, in South Korea. *Water* **2017**, *9*, 261. [[CrossRef](#)]
77. Jeong, S.; Ko, J.; Kang, M.; Yeom, J.; Ng, C.T.; Lee, S.H.; Lee, Y.G.; Kim, H.Y. Geographical variations in gross primary production and evapotranspiration of paddy rice in the Korean Peninsula. *Sci. Total Environ.* **2020**, *714*, 136632. [[CrossRef](#)]